The Effects of Estrogen Deficiency on Cortical Bone Microporosity and Mineralization

Divya Sharma, **Adriana I. Larriera**, **Paolo E. Palacio-Mancheno**, **Vittorio Gatti**, **J. Christopher Fritton**[a], **Timothy G. Bromage**[b], **Luis Cardoso**, **Stephen B. Doty**[c], and **Susannah P. Fritton**[*]
Department of Biomedical Engineering, The City College of New York, New York, NY 10031

[a]Department of Orthopaedics, New Jersey Medical School, Rutgers University, Newark, NJ 07103

[b]Department of Biomaterials, New York University College of Dentistry, New York, NY 10010

[c]Research Division, Hospital for Special Surgery, New York, NY 10021

Abstract

Recent studies have demonstrated matrix-mineral alterations in bone tissue surrounding osteocytes in estrogen-deficient animals. While cortical bone porosity has been shown to be a contributor to the mechanical properties of bone tissue, little analysis has been done to investigate the effects of estrogen deficiency on bone's microporosities, including the vascular and osteocyte lacunar porosities. In this study we examined alterations in cortical bone microporosity, mineralization, and cancellous bone architecture due to estrogen deficiency in the ovariectomized rat model of postmenopausal osteoporosis. Twenty-week-old female Sprague-Dawley rats were subjected to either ovariectomy or sham surgery. Six weeks post-surgery tibiae were analyzed using high-resolution micro-CT, backscattered electron imaging, nanoindentation, and dynamic histomorphometry. Estrogen deficiency caused an increase in cortical bone vascular porosity, with enlarged vascular pores and little change in tissue mineral density in the proximal tibial metaphysis. Measurements of cancellous architecture corresponded to previous studies reporting a decrease in bone volume fraction, an increase in trabecular separation, and a decrease in trabecular number in the proximal tibia due to estrogen deficiency. Nanoindentation results showed no differences in matrix stiffness in osteocyte-rich areas of the proximal tibia of estrogen-deficient rats, and bone labeling and backscattered electron imaging showed no significant changes in mineralization around the vascular pores. The findings demonstrate local surface alterations of vascular pores due to estrogen deficiency. An increase in cortical vascular porosity may diminish bone strength as well as alter bone mechanotransduction via interstitial fluid flow, both of which could contribute to bone fragility during postmenopausal osteoporosis.

[*]**Corresponding author:** Susannah P. Fritton, Ph.D., Department of Biomedical Engineering, The City College of New York, 160 Convent Avenue, New York, NY 10031, Phone: 212-650-5213, Fax: 212-650-6727, fritton@ccny.cuny.edu.

1. Introduction

Estrogen protects the skeleton from bone loss by suppressing turnover and maintaining a balance between bone formation and resorption [1]. Estrogen deficiency after menopause can lead to osteoporosis and an increased risk of bone fracture. While there are many studies in humans and rats that report a decrease in bone volume fraction due to estrogen deficiency, especially in cancellous bone, only recently have high-resolution analyses been performed to assess changes in bone microporosity, including the vascular porosity that houses the bone vasculature and the lacunar porosity that houses osteocytes [2–4].

The vascular pores in cortical bone play an important role in load-induced interstitial fluid flow because they allow relaxation of fluid pressure in the lacunar-canalicular pores when bone is mechanically loaded [5, 6]. Measurements of strain-generated potentials in bone specimens undergoing cyclic loading demonstrate that local spatial voltage gradients, which correspond to the pressure gradients that drive fluid flow, are 10 to 30 times greater near vascular canals compared to the spatial gradients across a whole bone specimen [7]. Theoretical models that include vascular pores clearly demonstrate that the primary relaxation of the excess bone fluid pressure occurs from the lacunar-canalicular system emptying into the vascular pores [8, 9].

In addition to providing conduits for interstitial fluid flow, the cortical microporosities associated with the vascular and lacunar-canalicular systems also contribute to the overall mechanical properties of bone tissue [10–13]. In humans, the loss of cortical rather than trabecular bone has been shown to predominate in cases of radial fracture [14]. Increase of cortical porosity due to aging has also been linked to loss of bone strength [15]. Because of the important contributions of cortical porosity to bone strength as well as to the transport of nutrients and removal of waste products to maintain bone cell function, changes in cortical microporosity, including the vascular and lacunar porosities, should be evaluated during diseases such as osteoporosis.

The distribution of bone matrix mineral, which also contributes to the mechanical quality of bone, has been shown to be altered with estrogen deficiency [16]. Matrix mineralization has been shown to be reduced in osteoporotic patients [17, 18]. However, there are contradictory findings related to bone mineralization changes after a drop in estrogen levels in rats, with some studies reporting no changes and others reporting reduced bone stiffness and hardness [19, 20].

Our recent studies using high-resolution microscopy demonstrate that estrogen deficiency alters the submicron lacunar-canalicular porosity surrounding osteocytes in cortical and cancellous bone [21]. We found that the increase in effective canalicular size measured using a small molecular weight tracer in ovariectomized rats was due to nanostructural matrix-

mineral changes at the osteocyte lacunar-canalicular surface. We have also found changes in molecular transport due to mechanical loading in the rat ovariectomy model [22].

The objective of this study was to further our investigations into how estrogen deficiency affects bone interstitial fluid pathways by assessing cortical microporosity and mineralization in the ovariectomized rat model of postmenopausal osteoporosis. Several high-resolution techniques were utilized to assess bone alterations, including 3D assessment of cortical bone vascular porosity and osteocyte lacunar porosity using micro-CT [23], assessment of mineralization density around vascular pores using backscattered electron imaging, and assessment of matrix stiffness using nanoindentation. Cancellous bone architectural changes due to estrogen deficiency were also measured, and bone turnover was quantified using fluorescent bone labels.

2. Materials and Methods

2.1 Animal model

The ovariectomized rat model of postmenopausal osteoporosis [24] was used to investigate the effects of reduced estrogen levels on bone microporosity, microarchitecture, and mineralization. Skeletally mature, 20-week-old rats were used because the rate of bone turnover in the proximal tibia at that age is very low [25]. All procedures were approved by the Institutional Animal Care and Use Committee.

At 20 weeks of age, female Sprague Dawley rats (Harlan Laboratories) were either subjected to ovariectomy (OVX, n=18) or to a sham surgery consisting of exposure of the ovaries without removal (SHAM, n=18). The animals were fed ad libitum for one week after surgery, and then the OVX group was pair-fed to the average food intake of the SHAM group (20 g standard rat chow per day). A subset of the animals (n=12 in the OVX group and n=12 in the SHAM group) received two bone formation markers via the intraperitoneal (IP) cavity at 11 days and 3 days before sacrifice (15 mg/kg calcein and 90 mg/kg xylenol orange, respectively) to assess histomorphometric indices of bone formation rate, mineral apposition rate, and percent mineralizing surfaces.

Six weeks after surgery (at 26 weeks of age) all animals were sacrificed, and uterine horns were weighed to assess the effectiveness of ovariectomy. Tibiae were harvested and either put immediately in 10% neutral buffered formalin for 48 hours or frozen at −20 °C. The analysis focused on the cortical and cancellous bone of the proximal tibial metaphysis because our recent studies demonstrated alterations in the lacunar-canalicular porosity surrounding osteocytes in this region [21, 22]. Tibiae from a subset of animals were used for three analyses: a micro-CT analysis to assess cortical microporosity and cancellous microarchitecture, a backscattered electron imaging and nanoindentation analysis to assess mineralization, and a histomorphometry analysis to assess bone turnover, as detailed below.

2.2 Micro-computed tomography imaging

Tibiae were scanned using a high-resolution micro-CT system (SkyScan 1172, Bruker microCT) to quantify cortical vascular and lacunar porosities, tissue mineral density (TMD), and cancellous microarchitecture (OVX: n=6; SHAM: n=6). Before scanning, the bones

were immersed in phosphate buffered saline and brought to room temperature in a custom low X-ray attenuation plastic holder that held each bone in place during scanning. For cortical microporosity and TMD measurements, images of the proximal tibiae were acquired with a voxel size of 1 μm ("1-μm scans") and for cancellous measurements images were acquired with a voxel size of 4 μm ("4-μm scans"). A 10-MP digital detector, 10-W power energy setting (100 kV and 100 μA), and a 0.5-mm aluminum filter were used, as in our previous work [23]. The 1-μm scans had a limited field of view due to the high resolution, thus requiring separate scans for the anterior and posterior regions of the proximal tibia, whereas the 4-μm scans allowed imaging the entire tibia. For all scans, X-ray projections were generated from the sample every 0.3 degrees, with the projections averaged 5 times to produce high-contrast, low-noise images. Hydroxyapatite rods (2-mm radius, densities of 0.25 and 0.75 g/cm^3 hydroxyapatite) were also scanned at l-μm voxel size to calibrate for TMD.

A modified back-projection reconstruction algorithm (NRecon v.1.6.5, Skyscan, Bruker microCT) was used to generate cross-sectional images from the X-ray projections. Images were optimized using a standard post-alignment compensation algorithm, treated with a Gaussian smoothing filter (kernel=4 pixels for 1-μm scans, and 1 pixel for 4-μm scans), and corrected for ring artifacts and beam hardening. All parameters except post-alignment compensation were set identically for all samples with the same voxel size.

2.3   Quantification of cortical vascular and lacunar porosities and TMD using micro-CT

Cortical bone microporosity was measured for the 1-μm scans utilizing a methodology previously developed in our laboratory to accurately assess cortical features, including vascular canals and osteocyte lacunae [23]. The scans were segmented using a global thresholding procedure to exclude soft tissue, with the threshold value (0.45 g/cm^3) chosen by analyzing the SHAM images with an edge detection algorithm to accurately segment cortical pore edges [23]. Cortical bone from the metaphysis of the proximal tibia was selected as the anatomical region of interest, starting 1 mm distal to the most distal point of the growth plate (**Fig. 1**).

Cortical vascular canal porosity (%), vascular canal diameter (μm), osteocyte lacunar porosity (%), lacunar volume (μm^3), and lacunar density were calculated in both the anterior and posterior regions of the proximal tibia using two cylindrical volumes of interest (VOIs) (diameter 250 μm, height 2 mm) for each region. All the cortical pores were identified using a "sphere fitting" algorithm (CTAn v. 1.11.0, SkyScan, Bruker microCT) and separated by volume. As in our previous work, osteocyte lacunae were isolated using a 3D despeckled filter that removed objects outside the range of 100 μm^3 to 600 μm^3 in volume (**Fig. 2**) [23]. Some of the cortical bone analyses from the SHAM group were previously reported in an analysis of the effect of micro-CT resolution and threshold method on the 3D assessment of cortical bone porosity [23].

The tissue mineral density was calculated for the 1-μm scan VOIs using the density calibration values obtained from the hydroxyapatite rod scans.

2.4 Assessment of cancellous bone microarchitecture using micro-CT

Cancellous bone measurements were performed for the 4-μm scans in a region of interest starting 1 mm distal to the proximal tibia growth plate to avoid primary spongiosa [26]. VOIs (2 mm height) were manually drawn to separate cancellous from cortical bone. Samples were segmented using a global threshold to exclude soft tissue, chosen by analyzing the SHAM images with an edge detection algorithm. The same segmentation threshold was applied to all scans, and noise was removed using the despeckle function **(Fig. 3).** Bone volume fraction (BV/TV), trabecular thickness (Tb.Th), trabecular separation (Tb.Sp), trabecular number (Tb.N), and structure model index (SMI) were calculated for the selected VOIs for SHAM and OVX.

2.5 Histomorphometric analysis of bone turnover

For cortical bone histomorphometric analysis, formalin-fixed, undecalcified tibiae were embedded in PMMA. Cortical cross-sections (120 μm thickness) were cut from the proximal metaphysis ~2 mm distal to the growth plate using a sawing microtome (Leica Instruments), polished to a final thickness of 70 μm, and then coverslipped. Dynamic histomorphometric parameters were measured using a bone-specific image analysis system (OsteoMeasure, OsteoMetrics Inc.). To assess bone formation rates, the following parameters were measured and calculated: double-labeled surface (dLS/BS, %); single-labeled surface (sLS/BS, %); mineralizing surface (MS/BS, %); mineral apposition rate (MAR, μm/day), calculated as the distance between double labels divided by interval labeling time; and bone formation rate (BFR/BS, $\mu m^3/\mu m^2/day$), calculated as MAR×MS/BS. For surfaces displaying a single label, the MS/BS value was recorded, while for those displaying double labels, MAR and BFR values were documented. Mineralizing vascular pores were quantified by counting fluorescently labeled vascular pores throughout the tibial cortex. Pores with 50% or more of their perimeter labeled with the calcein label were considered to be stained and were divided by the total number of vascular pores to obtain the percent mineralizing vascular pores.

2.6 Assessment of mineralization using backscattered electron imaging

To further analyze bone mineralization surrounding vascular pores, proximal tibial cross-sections from a subset of animals were analyzed using backscattered electron imaging (OVX: n=6; SHAM: n=6). Tibial specimens were embedded in PMMA, and blocks cut approximately 2 mm distal to the proximal growth plate were polished to a surface finish of 1 μm and carbon-coated to prepare for backscattered electron imaging [27]. Samples were scanned at 500-nm pixel resolution using a Zeiss EVO 50 scanning electron microscope at 50 Pa pressure, 15 kV accelerating voltage, 600 pA current, and approximately 9 mm working distance; carbon coating mitigated anomalies associated with charging and increased signal over higher pressures. Entire cross sections were acquired by automated Zeiss montaging software (SmartStich).

Regions of interest surrounding vascular pores were selected individually from image crosssections and stored as bmp files (**Fig. 4**). The grayscale values were then corrected using phantom images taken during the backscattered electron imaging to give a calibrated grayscale image. The mineral density surrounding each vascular pore was analyzed using Matlab code to segment the pixels surrounding each pore into twenty concentric 1-μm thick

rings and calculate the average grayscale value of each ring. Approximately 100 vascular pores were analyzed for each cross-section and then averaged for each animal.

2.7 Assessment of bone matrix stiffness using nanoindentation

Nanoindentation was performed to assess matrix stiffness in osteocyte-rich areas of the proximal tibia. Tibiae frozen at -20 °C (OVX: n=6; SHAM: n=6) were thawed and cut using a diamond blade saw (Buehler) at the proximal metaphysis ~2 mm distal to the growth plate. Specimens were then placed in peel-away molds and filled with an epoxy resin (Loctite Medical Epoxy, M-21HP, Hysol), which does not infiltrate the tissue but merely holds it in place. The embedded specimens were polished first using silicon carbide abrasive papers of decreasing grit sizes (600, 800, and 1200 grit) under deionized water, then with 0.5 and 0.25 µm diamond bead suspension solution and sonicated between each polishing step to remove debris. Samples were then dehydrated overnight at room temperature before testing.

Load-control nanoindentation tests were performed on dry specimens using a TriboIndenter nanoindenter (Hysitron, Inc.) [28]. A pyramidal-shaped Berkovich diamond tip indenter was calibrated using fused quartz crystals prior to testing. Load was applied at a constant rate by driving the indenter into the bone specimen. The maximum load (P_{max} =10 mN) was held on the sample for 10 seconds to minimize effects of viscoelastic deformation of the specimen, and the indenter was then unloaded at the same rate used in the loading step. Before proceeding to the next indent, the indenter was held on the surface of the specimen for approximately 100 seconds to establish thermal drift.

For each tibia specimen, two matrices of 25 indents, 5 µm apart, were made in the anterior and posterior regions of the cortical proximal metaphysis (**Fig. 5**). The indents were each ~800 nm wide. The elastic modulus and hardness were measured in an osteocyte-rich area, which was identified using the optical microscope installed in the nanoindenter system. The load-displacement data from each indentation were used to calculate the elastic modulus and hardness using the Oliver and Pharr method [29], with the Poisson's ratio of bone taken to be 0.3 [30, 31].

2.8 Statistical analysis

Differences between cortical microporosity measures and mineralization measures were assessed using two-way repeated-measures ANOVA for treatment (SHAM and OVX) and anatomical location followed by Bonferroni's multiple comparison tests with a significance level of $p < 0.05$. Differences in cancellous bone measures and bone histomorphometric measures as well as body weights and uterine horn weights were assessed using the two-sided Student's t-test with a significance level of $p < 0.05$. All the statistical analyses were performed using Prism 6 statistics software (GraphPad Software Inc.).

3. Results

The effectiveness of ovariectomy was verified by the absence of ovaries and by the reduced weight of the uterine horns in the OVX group (0.16 ± 0.034 g) compared to SHAM (0.75 ± 0.31 g), $p < 0.05$. Despite pair-feeding, at the time of sacrifice the OVX rats weighed more (291 ± 16 g) than the age-matched SHAM rats (243 ± 18 g), $p < 0.05$.

Cancellous bone of the proximal tibial metaphysis was considerably reduced in the OVX group over the 6-week time course of the experiment (**Fig. 6**). Bone volume fraction decreased by 60% in OVX compared to SHAM, and trabecular thickness was somewhat reduced for OVX (−12%). Trabecular separation was higher for OVX (+44%) and trabecular number was lower (−55%) compared to SHAM. The structure model index was higher in OVX (+42%) compared to SHAM (**Fig. 6**).

Estrogen-deficient rats demonstrated larger cortical vascular pores in both the anterior and posterior regions of the tibial metaphysis. High-resolution 3D micro-CT measurements demonstrated that the vascular canal porosity was significantly higher in OVX compared to SHAM for both the anterior (+28%) and posterior (+134%) regions (**Fig. 7a**). An increase in average vascular canal diameter due to estrogen deficiency was also found in both the anterior (+71%) and posterior (+57%) regions (**Fig. 7b**), while an increase in vascular canal separation was only found in the anterior region (+18%, **Fig. 7c**).

The remaining cortical bone features measured using micro-CT were not significantly altered in the estrogen-deficient animals: the osteocyte lacunar porosity and lacunar density were not significantly different between SHAM and OVX (**Fig. 7d-e**). In addition, there were no differences in the average lacunar volume (anterior region: SHAM: 217.8 ± 18.7 μm^3, OVX: 210.9 ± 5.0 μm^3; posterior region: SHAM: 216.5 ± 2.1 μm^3, OVX: 215.7 ± 2.9 μm^3).

Dynamic fluorochrome-based parameters were higher on the endocortical surfaces in the estrogen-deficient group. Bone formation rate and mineral apposition rate increased by 87% and 41%, respectively, on the endocortical surface in the OVX group (**Table 1**). On the periosteal surface there was no increase in mineralizing surface due to OVX (**Table 1**). A non-significant trend was observed for percent mineralizing vascular pores in estrogen-deficient rats (**Table 1**, p = 0.072).

The mineralization and nanoindentation analyses showed little differences in the SHAM and OVX groups. TMD measured with micro-CT showed a small (−4%) but significant difference in OVX compared to SHAM in the posterior tibial cortex and no difference in the anterior tibial cortex (**Fig. 7f**). The mineralization around vascular pores measured with backscattered electron imaging was not altered due to OVX (**Fig. 8**). The nanoindentation analysis demonstrated that the elastic modulus and hardness of osteocyte-rich areas of the proximal tibia were also unaltered due to estrogen deficiency (**Table 2**).

4. Discussion

The 3D quantification of cortical microporosities performed in this study demonstrates that estrogen deficiency causes an increase in cortical vascular porosity and increased cortical vascular canal diameter in the rat proximal tibia. While estrogen deficiency decreased cancellous bone volume fraction in the tibial metaphysis, osteocyte lacunar porosity and density were not significantly different in the OVX group compared to SHAM controls. The tissue mineral density of cortical bone showed little difference between SHAM and OVX groups, and nanoindentation results showed no differences in matrix stiffness in osteocyte-

rich areas of the proximal tibia of the estrogen-deficient rats. In addition, no significant differences were found in mineralization around vascular pores in the region analyzed. The results demonstrate local surface alterations of the cortical vascular pores due to estrogen deficiency and suggest that the nanostructural matrix-mineral level changes that we had previously observed in the osteocyte lacunar-canalicular porosity of estrogen-deficient rats [21] are indeed due to alterations occurring on the matrix surfaces surrounding osteocytes, and not because of altered matrix mineralization due to increased bone turnover.

The high-resolution micro-CT 3D renderings enabled the visualization of the structure of the cortical vascular pores for both sham-operated and estrogen-deficient animals. While there are few high-resolution analyses of cortical pores for estrogen-deficient rodents, the cortical vascular porosity of the SHAM group ($4.76 \pm 1.2\%$, anterior region; $1.27 \pm 0.24\%$ posterior region) falls within the range of values reported for the tibia and femur of untreated mice and rats (1–6%) using high-resolution desktop micro-CT and synchrotron radiation micro-CT [3, 4, 32–34]. The average canal diameter for the SHAM group (14.7 ± 1.9 μm, anterior region; 8.22 ± 1.0 μm, posterior region) is also similar to the values of canal diameter reported for the tibia and femur of untreated mice and rats (10–18 μm) [3, 4, 32, 33].

The enlargement of the cortical vascular porosity due to OVX seems to be a result of loss of matrix surrounding the vascular pores and not from an increase in newly laid down, unmineralized bone that would not be detected by micro-CT. Mineral apposition and bone formation rates were increased in OVX rats at the endocortical surfaces 6-weeks post-surgery, and higher bone turnover experienced by OVX rats can increase the amount of newly deposited bone that would first go through a phase of rapid primary mineralization and a slower secondary mineralization phase [35]. Yet both the dynamic histomorphometry and the backscattered electron imaging showed no significant changes in mineralization around the vascular pores in the regions analyzed. In addition, the overall TMD of the cortical bone demonstrated little change due to OVX. The enlargement of existing cortical pores rather than an increase in the number of pores is similar to findings of age-related changes in human long bones, where an increased pore size with increasing age has been found and has been suggested to occur due to focal remodeling on the vascular pore surface [36, 37]. The mechanism of the enlargement of the cortical pores (e.g., via osteoclast resorption or osteocyte-mediated matrix degradation) should be further investigated.

The clinical implications of enlarged cortical pores are that they could contribute to the degradation of bone's mechanical properties. The size and orientation of vascular channels have been demonstrated to contribute to bone strength and resistance to fracture [13]. A recent study in mice demonstrates a link between the intracortical canal network and work to fracture [38]. In addition, alterations in the vascular porosity have the potential to affect mechanotransduction. Modeling studies have shown that larger vascular pores reduce the interstitial fluid velocities around the pores [8]. The increase in vascular porosity demonstrated here in estrogen-deficient rats could both decrease bone strength and decrease the mechanical stimulus that osteocytes near the vascular pores would perceive. In addition to other matrix changes previously documented in the osteocyte lacunar-canalicular system due to estrogen deficiency [21], it is possible that these vascular pore changes could

contribute to bone degradation via the disruption of mechanical signals from the whole bone level down to the osteocyte [39, 40].

While estrogen deficiency increased the cortical vascular porosity in the tibial metaphysis, osteocyte lacunar porosity, average lacunar volume, and lacunar density were not significantly different in the OVX group compared to SHAM. We found similar results and similar osteocyte density values using confocal microscopy assessment of the rat OVX model of postmenopausal osteoporosis [21], and the average lacunar volumes in the present study are similar to synchrotron measurements in mice and rats [3, 33–34]. Using synchrotron micro-CT, Tommasini et al. also found no overall difference in lacunar porosity in the rat femur mid-diaphysis after 6 months of ovariectomy, but there was a decrease in lacunar volume and an increase in lacunar density for bone formed on the endosteal surface after ovariectomy [34]. Analysis of bone from patients having undergone osteoporotic fracture has also reported no change in osteocyte lacunar volume [41], while a reduction in osteocyte density has been shown in patients with osteoporotic vertebral fracture [42]. There is considerable evidence that osteocyte lacunar porosity is heterogeneous in both lacunar volume and alignment as well as lacunar density [4, 43]. It is also likely that osteocyte lacunar changes in the estrogen-deficient state are dependent on species and bone location, contributing to different findings among studies.

The cancellous bone analysis was performed to confirm changes reported in many studies using the rat model of postmenopausal osteoporosis, and all measures were consistent with previous reports. Cancellous bone volume fraction in the tibial metaphysis was significantly lower after OVX, similar to the decrease found in other studies [26, 44–46]. Trabecular thickness was somewhat smaller in OVX compared to SHAM, also consistent with previous results [26, 46]. Trabecular separation was higher for the OVX group compared to SHAM and trabecular number was significantly lower for OVX as previously reported [26, 44–46].

The nanoindentation analysis demonstrated that the elastic modulus and hardness were not altered due to estrogen deficiency, and the tissue mineral density of cortical bone showed little difference between SHAM and OVX groups. The values of elastic modulus and hardness found in the present study are similar to those found previously for normal and ovariectomized rats using nanoindentation [19, 47, 48]. In addition, the TMD values are similar to previous assessments of control and ovariectomized rats [46]. Several studies have shown that while estrogen deficiency causes a loss of bone mass in cancellous bone of rat vertebrae and proximal tibiae, the elastic and hardness properties of the remaining bone tissue are unchanged, similar to our findings [19, 47]. However, it is notable that other studies have shown that estrogen deficiency decreases elastic modulus in tibial cancellous bone in OVX rats [20], with little matrix mineralization changes in cortical bone of the proximal tibia, the region analyzed in the present study.

The degree of mineralization of bone tissue has been shown to be related to mechanical properties such as hardness and elastic modulus [49], yet the OVX group demonstrated no changes in matrix elastic modulus and hardness measured in osteocyte-rich regions of the tibial cortex. Thus, the nanoindentation results suggest that the matrix-mineral level changes around osteocytes observed in our previous study [21] are indeed alterations of the local

matrix surfaces surrounding osteocytes, and are not due to reduced mineralization of the OVX tissue because of increased bone turnover. While not measured in this study, the presence of a local mineral change at the lacunar-canalicular surface surrounding osteocytes after a drop in estrogen levels would suggest that osteocytes may play a role in mineral mobilization in postmenopausal osteoporosis, similar to what has been shown to occur during lactation [50]. A recent study that investigated the effects of lactation on bone mechanical properties found that an increase in the osteocyte lacunar-canalicular porosity produced a reduction in matrix elastic modulus measured using microindentation [51]. It is possible that canalicular changes previously demonstrated in the rat OVX model [21] could contribute to tissue-level changes that would be evident with microindentation analysis, where the indents are much larger and include lacunar and canalicular void space, but not with the nanoindentation analysis performed in the present study.

There are several limitations to this study. The ovariectomized rat model does not fully mimic the human condition of postmenopausal osteoporosis in that it produces osteopenia and not full-blown osteoporosis that could lead to bone fracture. In addition, most young adult rats have primary vascular pores, not secondary Haversian systems, although rats have been shown to have the capacity for intracortical remodeling [24]. However, the rat OVX model does have characteristics similar to that of postmenopausal bone loss, such as increased bone turnover, greater resorption than formation, and bone loss that is not uniform, with cancellous bone showing higher turnover than cortical bone [24]. Although our results appear to agree with previous synchrotron-measured findings, there are also limitations related to the quantification of lacunar porosity using the micro-CT scans and small differences may have gone undetected. The scanning rotation step (0.3 degrees), which is recommended for our micro-CT system, might lead to undersampling effects, potentially affecting the lacunar volume measurement. Although any such errors should be random and not affect one group over another, further investigation using higher resolution imaging with a better signal-to-noise ratio and smaller voxel size (e.g., synchrotron micro-CT) could be used to further assess lacunar volume changes due to estrogen deficiency. Another limitation is that the study did not assess potential alterations to the blood vessels inside the cortical pores due to estrogen deficiency. Future work should investigate the size and presence of blood vessels inside the cortical microporosity to further assess vascular pore changes. In addition, the mechanism of cortical pore enlargement due to estrogen deficiency should be further investigated. Finally, the study was limited to analysis of the proximal tibia. This region was chosen because of the documented changes due to estrogen deficiency [21, 43], but to more completely understand the bone degradation process during osteoporosis more anatomical regions should be studied.

In summary, this study successfully performed high-resolution 3D visualization and quantification of cortical microporosity and mineralization in the estrogen-deficient rat. We conclude that cortical bone vascular porosity is increased by estrogen deficiency, with ovariectomized rats demonstrating enlarged cortical pores in the tibial metaphysis. Together the results suggest that the nanostructural matrix-mineral level changes in the osteocyte lacunar-canalicular porosity of estrogen-deficient rats demonstrated in previous work [21] are indeed due to alterations occurring on the local matrix surfaces surrounding osteocytes, and not because of altered matrix mineralization due to increased bone turnover. The results

also demonstrate local surface alterations of the cortical vascular pores due to estrogen deficiency that could contribute to an increase of bone fragility due to decreased strength and decreased interstitial fluid flow because of the altered structure.

Acknowledgments

References

[1]. Almeida M, Han L, Martin-Millan M, Plotkin LI, Stewart SA, Roberson PK, Kousteni S, O'Brien CA, Bellido T, Parfitt AM, Weinstein RS, Jilka RL, Manolagas SC. Skeletal involution by age-associated oxidative stress and its acceleration by loss of sex steroids. J Biol Chem 2007;282: 27285–27297. [PubMed: 17623659]

[2]. Cooper D, Turinsky A, Sensen C, Hallgrimsson B. Effect of voxel size on 3D micro-CT analysis of cortical bone porosity. Calcif Tissue Int 2007;80: 211–19. [PubMed: 17340226]

[3]. Matsumoto T, Yoshino M, Asano T, Uesugi K, Todoh M, Tanaka M. Monochromatic synchrotron radiation muCT reveals disuse-mediated canal network rarefaction in cortical bone of growing rat tibiae. J Appl Physiol 2006;100: 274–80. [PubMed: 16141381]

[4]. Schneider P, Stauber M, Voide R, Stampanoni M, Donahue LR, Muller R. Ultrastructural properties in cortical bone vary greatly in two inbred strains of mice as assessed by synchrotron light based micro- and nano-CT. J Bone Miner Res 2007;22: 1557–70. [PubMed: 17605631]

[5]. Cowin SC. Bone poroelasticity. J Biomech 1999;32: 217–38. [PubMed: 10093022]

[6]. Fritton SP, Weinbaum S. Fluid and solute transport in bone: flow-induced mechanotransduction Annu Rev Fluid Mech 2009;41: 347–374. [PubMed: 20072666]

[7]. Starkebaum W, Pollack SR, Korostoff E. Microelectrode studies of stress-generated potentials in four-point bending of bone. J Biomed Mater Res 1979; 13: 729–751. [PubMed: 479219]

[8]. Wang L, Fritton SP, Cowin SC, Weinbaum S. Fluid pressure relaxation depends upon osteonal microstructure: modeling an oscillatory bending experiment. J Biomech 1999;32: 663–72. [PubMed: 10400353]

[9]. Goulet GC, Hamilton N, Cooper D, Coombe D, Tran D, Martinuzzi R, Zernicke RF. Influence of vascular porosity on fluid flow and nutrient transport in loaded cortical bone. J Biomech 2008;41: 2169–75. [PubMed: 18533159]

[10]. Martin RB. Determinants of the mechanical properties of bones. J Biomech 1991;24: 79–88. [PubMed: 1842337]

[11]. McCalden RW, McGeough JA, Barker MB, Court-Brown CM. Age-related changes in the tensile properties of cortical bone. The relative importance of changes in porosity, mineralization, and microstructure. J Bone Joint Surg Am 1993;75: 1193–205. [PubMed: 8354678]

[12]. Schaffler MB, Burr DB. Stiffness of compact bone: effects of porosity and density. J Biomech 1988;21: 13–6. [PubMed: 3339022]

[13]. Currey JD, Shahar R. Cavities in the compact bone in tetrapods and fish and their effect on mechanical properties. J Struct Biol 2013;183: 107–22. [PubMed: 23664869]

[14]. Spadaro JA, Werner FW, Brenner RA, Fortino MD, Fay LA, Edwards WT. Cortical and trabecular bone contribute strength to the osteopenic distal radius. J Orthop Res 1994;12: 211–8. [PubMed: 8164094]

[15]. Zebaze RM, Ghasem-Zadeh A, Bohte A, Iuliano-Burns S, Mirams M, Price RI, Mackie EJ, Seeman E. Intracortical remodelling and porosity in the distal radius and post-mortem femurs of women: a cross-sectional study. Lancet 2010;375: 1729–36. [PubMed: 20472174]

[16]. Kim G, Cole JH, Boskey AL, Baker SP, van der Meulen MC. Reduced tissue-level stiffness and mineralization in osteoporotic cancellous bone. Calcif Tissue Int 2014;95: 125–31. [PubMed: 24888692]

[17]. Loveridge N, Power J, Reeve J, Boyde A. Bone mineralization density and femoral neck fragility. Bone 2004;35: 929–41. [PubMed: 15454100]

[18]. Roschger P, Misof B, Paschalis E, Fratzl P, Klaushofer K. Changes in the degree of mineralization with osteoporosis and its treatment. Curr Osteoporos Rep 2014;12: 338–50. [PubMed: 24947951]

[19]. Guo XE, Goldstein SA. Vertebral trabecular bone microscopic tissue elastic modulus and hardness do not change in ovariectomized rats. J Orthop Res 2000;18: 333–6. [PubMed: 10815837]

[20]. Maimoun L, Brennan-Speranza TC, Rizzoli R, Ammann P. Effects of ovariectomy on the changes in microarchitecture and material level properties in response to hind leg disuse in female rats. Bone 2012;51: 586–91. [PubMed: 22580391]

[21]. Sharma D, Ciani C, Marin PA, Levy JD, Doty SB, Fritton SP. Alterations in the osteocyte lacunar-canalicular microenvironment due to estrogen deficiency. Bone 2012;51: 488–97. [PubMed: 22634177]

[22]. Ciani C, Sharma D, Doty SB, Fritton SP. Ovariectomy enhances mechanical load-induced solute transport around osteocytes in rat cancellous bone. Bone 2014;59: 229–34. [PubMed: 24316418]

[23]. Palacio-Mancheno PE, Larriera AI, Doty SB, Cardoso L, Fritton SP. 3D assessment of cortical bone porosity and tissue mineral density using high-resolution μCT: effects of resolution and threshold method. J Bone Miner Res 2014;29: 142–5. [PubMed: 23775635]

[24]. Kalu DN. The ovariectomized rat model of postmenopausal bone loss. Bone Miner 1991;15: 175–91. [PubMed: 1773131]

[25]. Horton JA, Bariteau JT, Loomis RM, Strauss JA, Damron TA. Ontogeny of skeletal maturation in the juvenile rat. Anat Rec (Hoboken) 2008;291: 283–92. [PubMed: 18228587]

[26]. Laib A, Kumer JL, Majumdar S, Lane NE. The temporal changes of trabecular architecture in ovariectomized rats assessed by MicroCT. Osteoporos Int 2001;12: 936–41. [PubMed: 11804020]

[27]. Goldman HM, Blayvas A, Boyde A, Howell PG, Clement JG, Bromage TG. Correlative light and backscattered electron microscopy of bone--part II: automated image analysis. Scanning 2000;22: 337–44. [PubMed: 11145258]

[28]. Kavukcuoglu NB, Patterson-Buckendahl P, Mann AB. Effect of osteocalcin deficiency on the nanomechanics and chemistry of mouse bones. J Mech Behav Biomed Mater 2009;2: 348–54. [PubMed: 19627841]

[29]. Oliver WC, Pharr GM. An improved technique for determining hardness and elastic modulus using load and displacement sensing indentation experiments. J Mater Res 1992;7: 1564–1583.

[30]. Rho JY, Roy ME, 2nd, Tsui TY, Pharr GM. Elastic properties of microstructural components of human bone tissue as measured by nanoindentation. J Biomed Mater Res 1999;45: 48–54. [PubMed: 10397957]

[31]. Zysset PK, Guo XE, Hoffler CE, Moore KE, Goldstein SA. Elastic modulus and hardness of cortical and trabecular bone lamellae measured by nanoindentation in the human femur. J Biomech 1999;32: 1005–12. [PubMed: 10476838]

[32]. Matsumoto T, Yoshino M, Uesugi K, Tanaka M. Biphasic change and disuse-mediated regression of canal network structure in cortical bone of growing rats. Bone 2007;41: 239–46. [PubMed: 17544983]

[33]. Britz HM, Jokihaara J, Leppanen OV, Jarvinen T, Cooper DM. 3D visualization and quantification of rat cortical bone porosity using a desktop micro-CT system: a case study in the tibia. J Microsc 2010;240: 32–7. [PubMed: 21050211]

[34]. Tommasini SM, Trinward A, Acerbo AS, De Carlo F, Miller LM, Judex S. Changes in intracortical microporosities induced by pharmaceutical treatment of osteoporosis as detected by high resolution micro-CT. Bone 2012;50: 596–604. [PubMed: 22226688]

[35]. Wronski TJ, Dann LM, Scott KS, Cintron M. Long-term effects of ovariectomy and aging on the rat skeleton. Calcif Tissue Int 1989;45: 360–6. [PubMed: 2509027]

[36]. Stein MS, Feik SA, Thomas CD, Clement JG, Wark JD. An automated analysis of intracortical porosity in human femoral bone across age. J Bone Miner Res 1999;14: 624–32. [PubMed: 10234585]

[37]. Perilli E, Bala Y, Zebaze R, Reynolds KJ, Seeman E. Regional heterogeneity in the configuration of the intracortical canals of the femoral shaft. Calcif Tissue Int 2015;97: 327–35. [PubMed: 26050153]

[38]. Schneider P, Voide R, Stampanoni M, Donahue LR, Muller R. The importance of the intracortical canal network for murine bone mechanics. Bone 2013;53: 120–8. [PubMed: 23219945]

[39]. Turner RT. Mechanical signaling in the development of postmenopausal osteoporosis. Lupus 1999;8: 388–92. [PubMed: 10455519]

[40]. Klein-Nulend J, van Oers RF, Bakker AD, Bacabac RG. Bone cell mechanosensitivity, estrogen deficiency, and osteoporosis. J Biomech 2015;48: 855–65. [PubMed: 25582356]

[41]. McCreadie BR, Hollister SJ, Schaffler MB, Goldstein SA. Osteocyte lacuna size and shape in women with and without osteoporotic fracture. J Biomech 2004;37: 563–72. [PubMed: 14996569]

[42]. Qiu S, Rao DS, Palnitkar S, Parfitt AM. Reduced iliac cancellous osteocyte density in patients with osteoporotic vertebral fracture. J Bone Miner Res 2003;18: 1657–63. [PubMed: 12968675]

[43]. van Hove RP, Nolte PA, Vatsa A, Semeins CM, Salmon PL, Smit TH, Klein-Nulend J. Osteocyte morphology in human tibiae of different bone pathologies with different bone mineral density--is there a role for mechanosensing? Bone 2009;45: 321–9. [PubMed: 19398046]

[44]. Westerlind KC, Wronski TJ, Ritman EL, Luo ZP, An KN, Bell NH, Turner RT. Estrogen regulates the rate of bone turnover but bone balance in ovariectomized rats is modulated by prevailing mechanical strain. Proc Natl Acad Sci U S A 1997;94: 4199–204. [PubMed: 9108129]

[45]. Yang J, Pham SM, Crabbe DL. High-resolution Micro-CT evaluation of mid- to long-term effects of estrogen deficiency on rat trabecular bone. Acad Radiol 2003;10: 1153–8. [PubMed: 14587633]

[46]. Brouwers JE, van Rietbergen B, Huiskes R, Ito K. Effects of PTH treatment on tibial bone of ovariectomized rats assessed by in vivo micro-CT. Osteoporos Int 2009;20: 1823–35. [PubMed: 19262974]

[47]. Lane NE, Yao W, Kinney JH, Modin G, Balooch M, Wronski TJ. Both hPTH(1–34) and bFGF increase trabecular bone mass in osteopenic rats but they have different effects on trabecular bone architecture. J Bone Miner Res 2003;18: 2105–15. [PubMed: 14672345]

[48]. Lewis G, Nyman JS. The use of nanoindentation for characterizing the properties of mineralized hard tissues: state-of-the art review. J Biomed Mater Res B Appl Biomater 2008;87: 286–301. [PubMed: 18395829]

[49]. Burket J, Gourion-Arsiquaud S, Havill LM, Baker SP, Boskey AL, van der Meulen MC. Microstructure and nanomechanical properties in osteons relate to tissue and animal age. J Biomech 2011;44: 277–84. [PubMed: 21074774]

[50]. Qing H, Ardeshirpour L, Pajevic PD, Dusevich V, Jahn K, Kato S, Wysolmerski J, Bonewald LF. Demonstration of osteocytic perilacunar/canalicular remodeling in mice during lactation. J Bone Miner Res 2012;27: 1018–29. [PubMed: 22308018]

[51]. Kaya S, Basta-Pljakic J, Seref-Ferlengez Z, Majeska RJ, Cardoso L, Bromage TG, Zhang Q, Flach CR, Mendelsohn R, Yakar S, Fritton SP, Schaffler MB. Lactation-induced changes in the volume of osteocyte lacunar-canalicular space alter mechanical properties in cortical bone tissue. J Bone Miner Res 2017;32: 688–97. [PubMed: 27859586]

Highlights

- Recent studies have demonstrated matrix-mineral alterations in bone tissue surrounding osteocytes in estrogen-deficient animals.

- This study assessed alterations in cortical bone microporosity and mineralization in the rat ovariectomy model of postmenopausal osteoporosis.

- Estrogen deficiency increased cortical vascular porosity, with enlarged cortical pores but no significant changes in mineralization around the pores.

- Nanoindentation results showed no differences in matrix stiffness in osteocyte-rich areas of the proximal tibia of estrogen-deficient rats.

- Findings provide evidence of local surface alterations of the vascular pores due to estrogen deficiency.
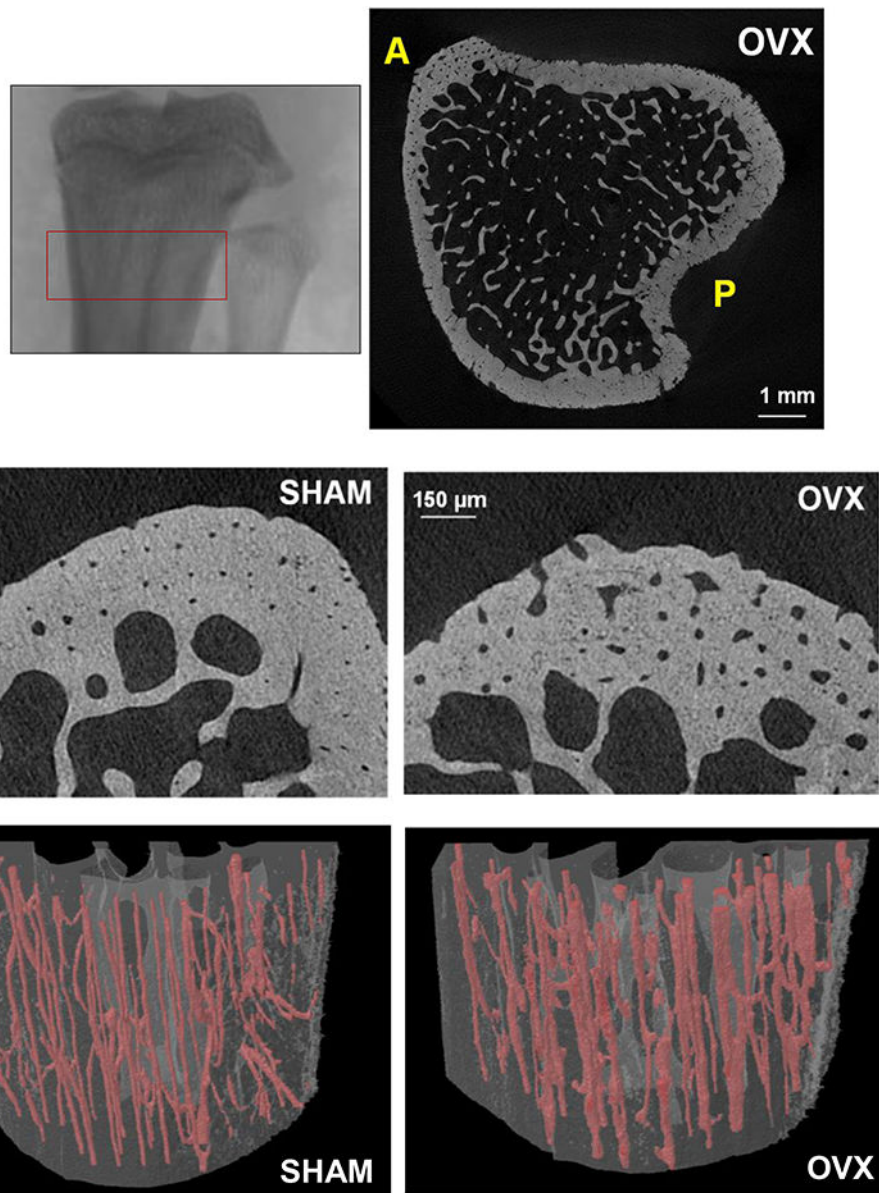
Figure 1.
Top left: Micro-CT image of the rat proximal tibia demonstrating region of analysis; longitudinal height of region = 2 mm. **Top right:** Cross-sectional image from region analyzed for an OVX rat; cortical vascular and lacunar porosities were assessed in the anterior (A) and posterior (P) regions. **Middle row:** Micro-CT cross-sectional images of the anterior proximal tibial metaphysis of a SHAM and OVX rat (1-μm voxel size). **Bottom row:** 3D renderings of cortical vascular canals in the anterior region for a SHAM and OVX rat (osteocyte lacunae not shown); longitudinal height of section = 2 mm.
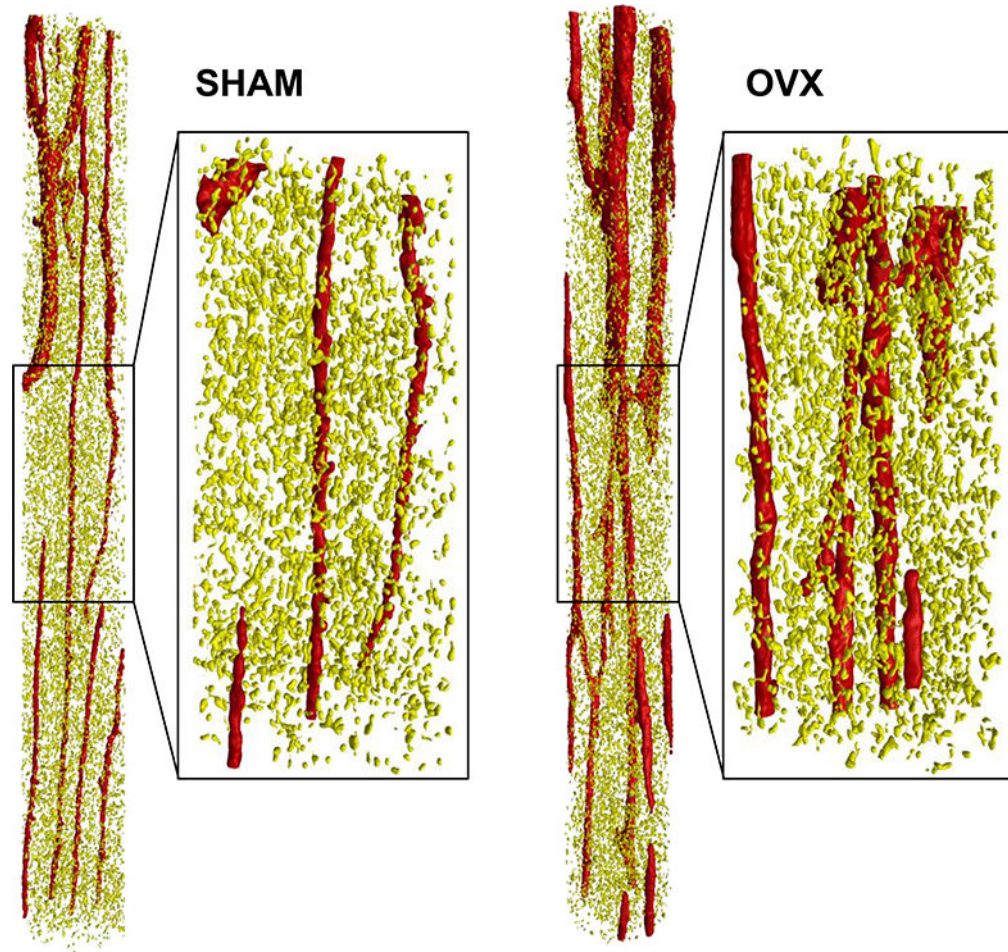
Figure 2.
Representative SHAM and OVX volumes of interests (VOIs) from the anterior proximal tibial metaphysis illustrating the segmentation of the cortical vascular canals (red) and osteocyte lacunae (yellow). The entire (unzoomed) cylindrical VOIs are 250 μm in diameter and 2 mm in height.
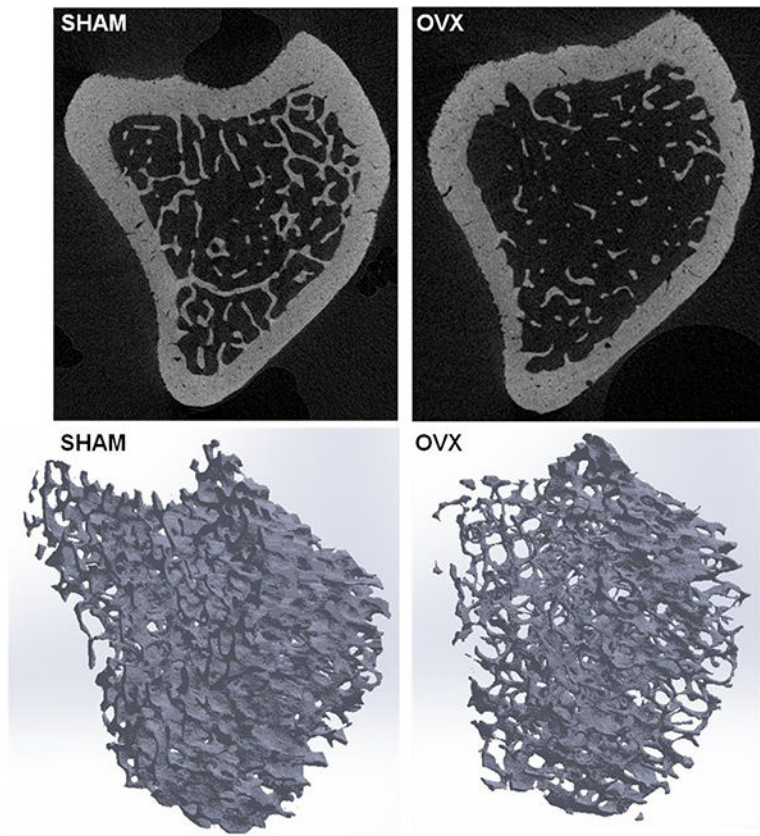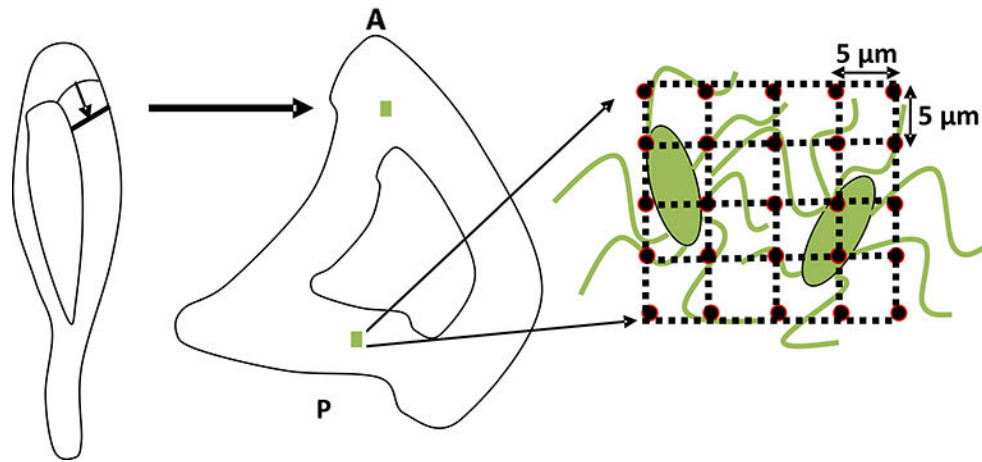
Figure 3.
Top row: Micro-CT cross-sectional images of the proximal tibial metaphysis of a SHAM and OVX rat (4-μm voxel size), taken from the same proximal tibia region analyzed for the cortical microporosities shown in Figure 1. **Bottom row:** Segmented volumes of interest (VOIs) used to assess the cancellous bone microarchitecture in SHAM and OVX; VOI height = 2 mm.
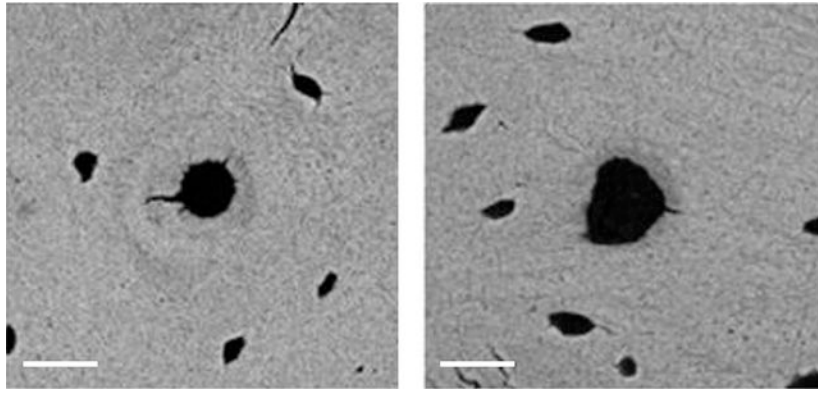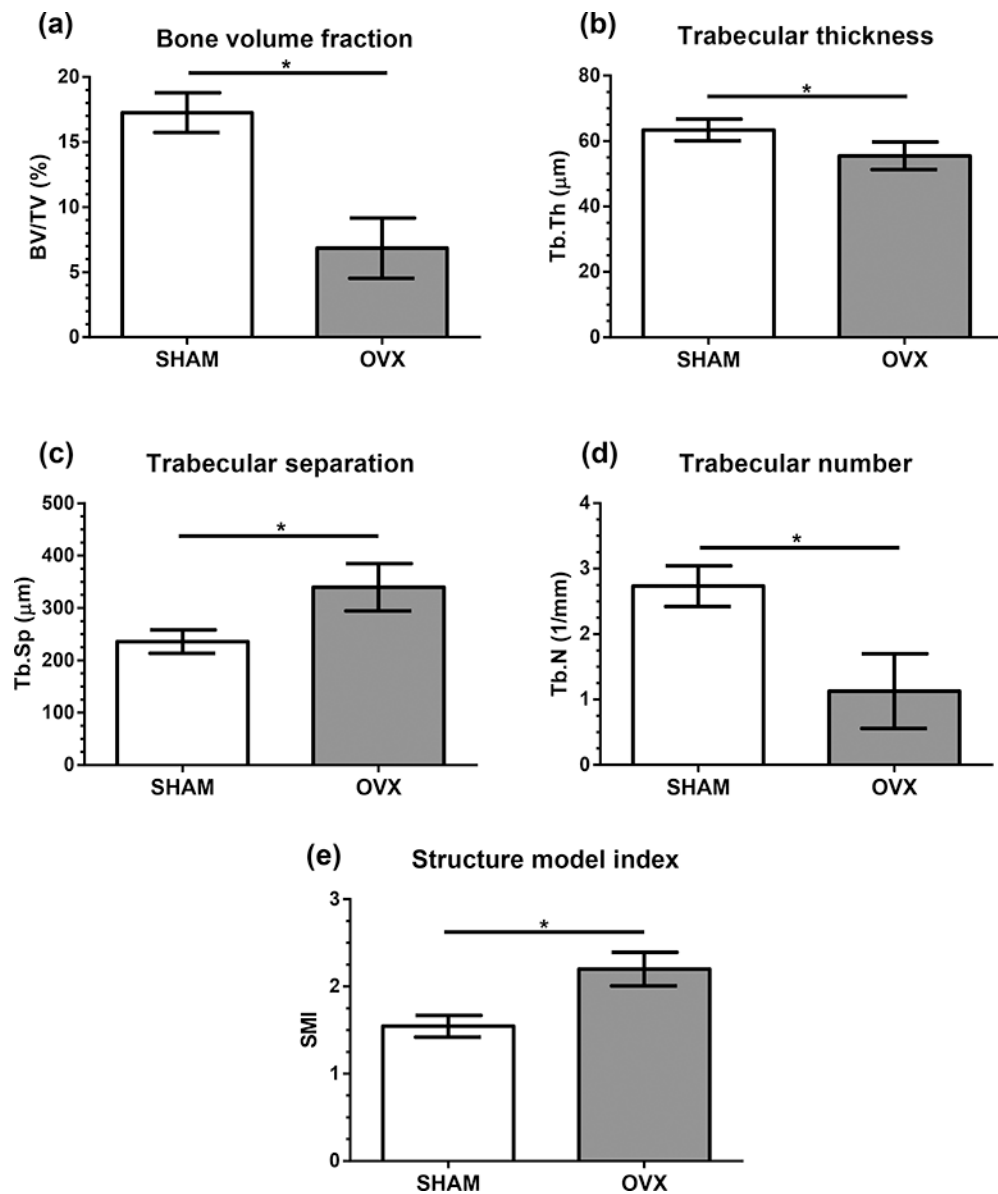
Figure 4.
Typical SEM images of a region of interest surrounding a vascular pore from a SHAM rat (**left**) and OVX rat (**right**). Both images taken from the posterior proximal tibia; scale bars = 20 μm.
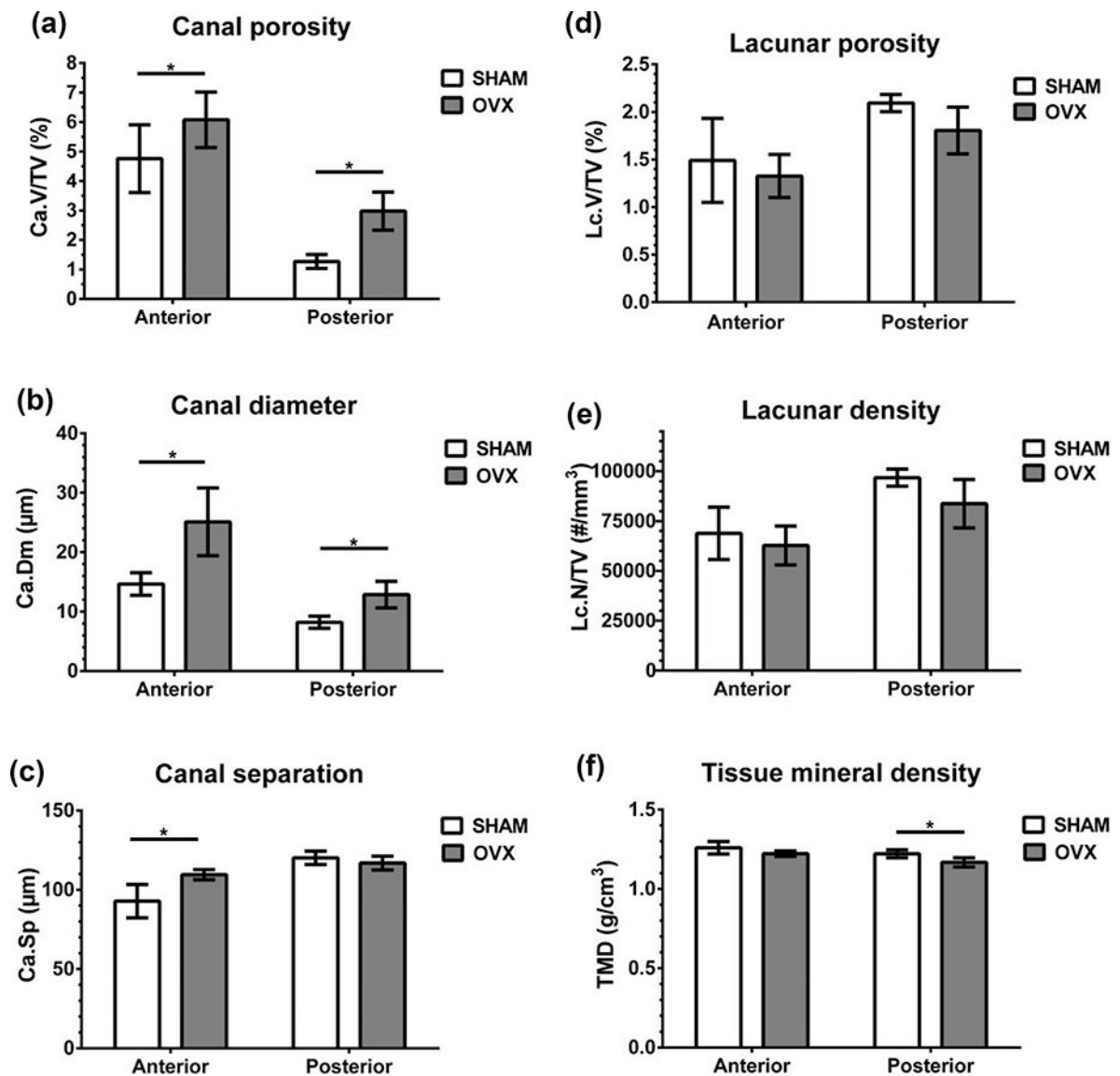
Figure 5.
A schematic representation of the rat tibia showing the regions analyzed using nanoindentation. A matrix of 25 nanoindents, 5 μm apart, was made in the anterior (A) and posterior (P) of the cortical tibial metaphysis in an osteocyte-rich area.
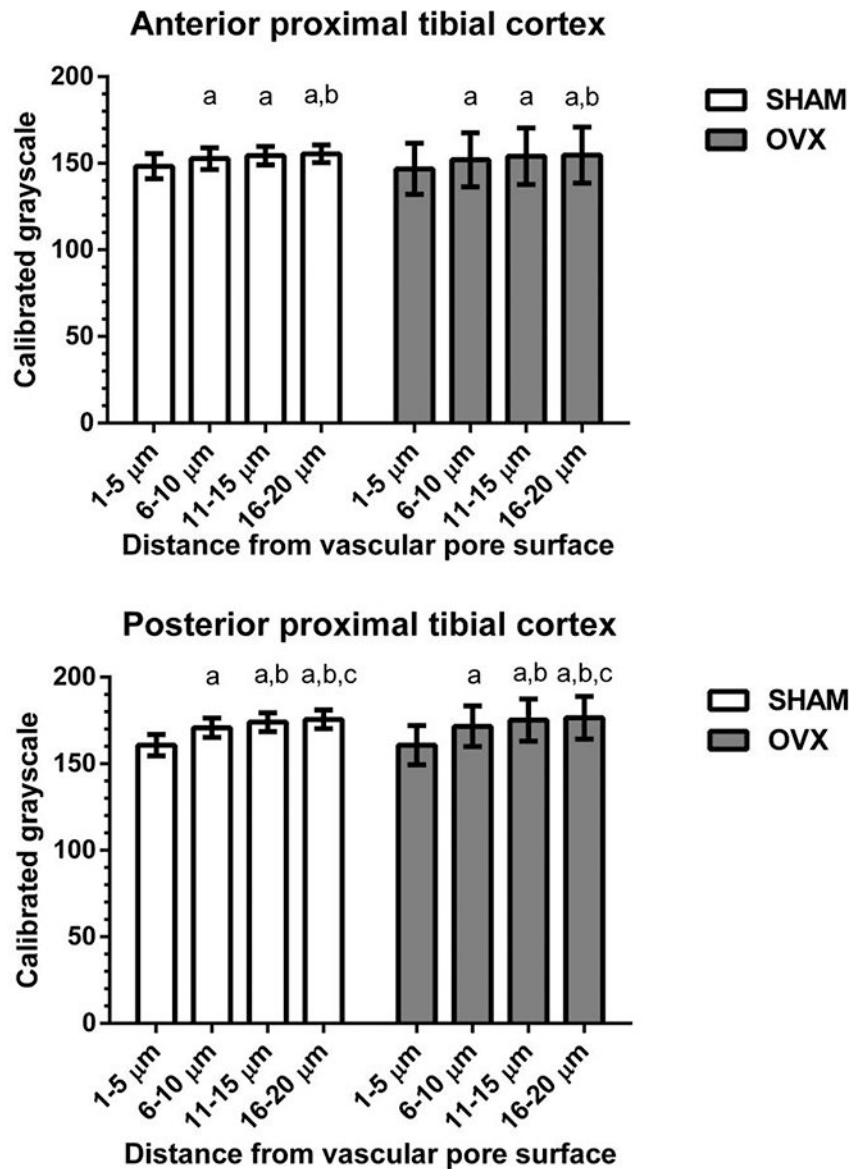
Figure 6.
Micro-CT microarchitectural measures (mean ± standard deviation) for cancellous bone from the proximal tibia metaphysis for SHAM and OVX groups. **(a)** Cancellous bone volume fraction, BV/TV (%). **(b)** Trabecular thickness, Tb.Th (μm). **(c)** Trabecular separation, Tb.Sp (μm). **(d)** Trabecular number, Tb.N (1/mm), **(e)** Structure model index, SMI. *$p < 0.05$.

Figure 7.
Micro-CT microarchitectural measures (mean ± standard deviation) for cortical bone from the anterior and posterior regions of the proximal tibia metaphysis for SHAM and OVX groups. **(a)** Vascular canal porosity, Ca.V/TV (%). **(b)** Average vascular canal diameter, Ca.Dm (μm). **(c)** Vascular canal separation, Ca.Sp (μm). **(d)** Osteocyte lacunar porosity, Lc.V/TV (%). **(e)** Osteocyte lacunar density, Lc.N/TV (# per mm^3). **(f)** Tissue mineral density, TMD (g/cm^3). *p < 0.05.

Figure 8.
SEM assessment of mineralization (calibrated grayscale, mean ± standard deviation) around vascular pores from the anterior (**top**) and posterior (**bottom**) regions of the proximal tibia cortex. For both SHAM and OVX, mineralization level was lowest at the vascular pore surface; but there were no mineralization differences between SHAM and OVX. [a] different from 1–5 μm region, $p < 0.05$; [b] different from 6–10 μm region, $p < 0.05$; [c] different from 11–15 μm region, $p < 0.05$.

Table 1.

Bone histomorphometric indices for cortical bone of the proximal tibia metaphysis. Values expressed as mean ± standard deviation. SHAM: sham-operated controls; OVX: ovariectomized.

	SHAM	OVX
Endocortical bone formation rate, Ec.BFR ($\mu m^3/\mu m^2$/day)	0.68 ± 0.20	1.27 ± 0.32[*]
Endocortical mineral apposition rate, Ec.MAR (μm/day)	1.62 ± 0.27	2.29 ± 0.44[*]
Periosteal mineralizing surface / bone surface (Ps.MS/BS) (%)	19.6 ± 6.5	22.5 ± 7.1
Mineralizing vascular pores (%)	16.3 ± 7.0	25.2 ± 12

[*] different from SHAM, p < 0.05

Table 2.

Elastic modulus and hardness values measured using nanoindentation in the anterior and posterior regions of cortical bone in the proximal tibia metaphysis. Values expressed as mean ± standard deviation. SHAM: sham-operated controls; OVX: ovariectomized.

	SHAM	OVX
Elastic modulus (GPa) Anterior region	22.9 ± 1.7	22.5 ± 1.8
Posterior region	23.6 ± 1.2	22.8 ± 2.9
Hardness (GPa) Anterior region	0.774 ± 0.060	0.761 ± 0.068
Posterior region	0.793 ± 0.054	0.820 ± 0.062